



Pretty-small four-port dual-wideband 28/38 GHz MIMO antenna with robust isolation and high diversity performance for millimeter-wave 5G wireless systems

Asma Khabba¹ · Jamal Amadid¹ · Saida Ibnyaich¹ · Abdelouhab Zeroual¹

Received: 28 October 2021 / Revised: 18 February 2022 / Accepted: 15 April 2022 / Published online: 10 May 2022
© The Author(s), under exclusive licence to Springer Science+Business Media, LLC, part of Springer Nature 2022

Abstract

The implementation of wireless technology at millimeter wave spectrum is becoming inevitable in the human life to keep pace with the urgent need of the high throughput and reliable transmission. In this research paper, a new miniaturized dual-wideband MIMO antenna has been suggested, and strictly studied for millimeter-wave 5G applications. The MIMO antenna is formed using four identical elements orthogonally placed on the low-loss RTRogers Duroid 5880 substrate with total area of $14 \times 14 \times 0.8 \text{ mm}^3$. Each element consists of an elliptical microstrip patch antenna with inset-feed and slotted ground plane, developed to provide dual band operation of 3 GHz (26.62–29.71 GHz) and 3.2 GHz (36.3–39.5 GHz) at the pioneer bands, namely 28 and 38 GHz respectively. The novelty of the suggested design resides in the inclusion of a new cross-shaped decoupling structure among elements in the upper and lower sides of the substrate to acquire severe isolation outstrips 30dB while retaining quite simple structure and very small size, besides desirable radiation traits, including high radiation efficiency exceeding 98%, reasonable gain up to 6.8 dB along with stable and directive patterns. Furthermore, the diversity performance of the MIMO antenna is also examined in terms of various essential metrics which are all significantly respected the agreed practical thresholds. The envelope correlation coefficient (ECC) is less than 0.0005, the diversity gain (DG) exceeds 9.99 dB, the total active reflection coefficient (TARC) is below -10 dB, the channel capacity loss (CCL) is no longer than 0.35 bits/s/Hz and high channel capacity (CC) reaches to 22 bits/s/Hz. A detailed comparison with the existing works confirmed that the intended design blends several essential qualities that already mentioned which making it a sought-after option for 5G terminals.

Keywords Elliptical antenna · 5G MIMO · Millimeter wave · Dual-wideband · Decoupling structure · Severe isolation

1 Introduction

Due to the fast progress of the universal telecommunication and the mobile communication systems, the 5G technology is now becoming in the spotlight to fulfil the fundamental demands regarding the colossal data rate for the modern wireless communications. Indeed, various technologies such as millimeter wave systems have been evolved to meet the high throughput requirement and will be integrated in the futuristic wireless devices and mobile networks. The

currently used wireless networks starting from 300 MHz to 3 GHz is choking up and has normally achieved its upper limit of exploitation owing to the large number of applications and there is no sufficient spectrum left for further upgrading beyond the fourth generation (4G) [1]. Several bands within the range 3–300 GHz has been defined by the Federal Communication Commission (FCC) to implement the 5G mobile networks and there are two prominent bands by reference to the scientific reports and studies [2–4], i.e. sub-6 GHz (3–6 GHz) and millimeter-wave (24–40 GHz) frequency bands. However, researchers are fascinated by the mmWave spectrum due to the abundant spectrum provided in this range. The essential purpose of the 5G networks is to allow the operators a reliable connectivity with high bandwidth, enhanced data rates and low latency. Such features would allow the rapid download of high-definition videos in addition to the promotion of other advanced technologies

✉ Asma Khabba
asma.khabba@edu.uca.ac.ma

¹ Instrumentation, Signals and Physical Systems (I2SP)
Team, Faculty of Sciences Semlalia, Cadi Ayyad University,
Marrakesh, Morocco

including the Internet of Things (IoT), the smart cities, self-driven vehicles, and healthcare systems, etc. These technologies might be achieved in an easy way by exploiting the mmWave spectrum [5]. Nevertheless, the employment of high frequency spectrum raises a set of major challenges regarding the free-space propagation. Among these challenges is the high sensitivity to the atmospheric attenuation, rain, snowfall, and fog, etc., which inherently results in high electromagnetic wave losses and bad wireless communications. Besides, the signal of high frequency spectrum suffers from a low penetration power, it can propagate for just a few miles compared to the low frequency signals and cannot break through the obstacle such as buildings, trees, etc. which may severely affect the strength and the quality of the signal during transmission and leads to smaller coverage zone [6]. Several scenarios have been discussed to tackle the propagation loss issues such the creation of small-cell base stations so-called femto-cells and pico-cells which also help to raise the frequency reuse [7]. Another key solution is the utilization of high gain and highly directive antennas which significantly improves the signal resistance to the atmospheric absorption [8]. On the other side, an experimental study [9] has been conducted to test the effect of the rain and atmospheric attenuation on the frequency spectrum between 0 and 400 GHz. It is found that the minimum atmospheric absorption is reached within the range 20–40 GHz while a maximum attenuation is noticed at 60 GHz, and 190 GHz, etc. Accordingly, the FCC has defined several pioneer bands around 28 and 38 GHz for 5G wireless systems, such as 26.5–29.5 GHz, 27.5–28.35 GHz, and 37–40 GHz. The Multi Input Multi Output (MIMO) antenna with broadband characteristic is deemed an imperative part to establish the transmission chain of the 5G wireless networks which enables higher data rates with improved spectrum efficiency and upgraded channel capacity by using the multipath channel and without increasing the antenna feeding power [10, 11].

Various 5G MIMO antenna designs operating at the mmWave targeted bands have been recently reported in the literature. As an example, in Ref. [1], authors have proposed an HP-shaped four-element MIMO antenna working in the range of 37–40 GHz. The proposed design showed a wideband characteristic, however the total area was $32.5 \times 32.5 \text{ mm}^2$ which is rather large, while the isolation was just 15dB. In Ref. [3], an E-shaped quad-element MIMO antenna resonating at 28/38GHz has been presented. The MIMO antenna presents a compact size of $20 \times 24 \text{ mm}^2$, but the bandwidth obtained was relatively small for the 5G applications. In addition, only the envelope correlation coefficient (ECC) has been analysed to evaluate the MIMO performances. In Ref. [7], a hexagonal-shaped wire antenna array has been designed to be used at 28 GHz. A wide bandwidth from 25 to 34.9 GHz has been provided. Nevertheless, the array had a relatively large dimensions of

$45 \times 20 \text{ mm}^2$ and the vias employment has raised the design complexity. In Ref. [8], a four-port C-shaped MIMO antenna with total dimensions of $30 \times 35 \text{ mm}^2$ has been implemented to operate along a wide spectrum of 25.5–29.6 GHz. However, the minimum ports-isolation achieved was just 10dB and the occupied dimensions is still somewhat significant. In Ref. [10], a dual-port substrate integrated waveguide (SIW) MIMO antenna has been proposed for 28 GHz mm-wave applications. The design was marked by good gain of 6.9 dB and isolation more than 17dB. Nonetheless, a small bandwidth of 0.4 GHz was attained. In Ref. [11], 4-element infinity-shaped MIMO antenna has been suggested to operate at 28 GHz. The MIMO elements have been placed orthogonally to achieve high isolation with 2 GHz of bandwidth. However the total size was $30 \times 30 \text{ mm}^2$ which can be further reduced to accommodate the small wireless devices. In Ref. [12], a tree-shaped quad-element MIMO antenna working at mmWave spectrum has been investigated. The antenna-element was bearing a huge bandwidth from 23 to 40 GHz. But, the bulky dimensions taken up by the reported design constitute its limitation. In Ref. [13], a 4-port circular polarization MIMO antenna design with small size and wide bandwidth of 25–29.6 GHz has been carried out. However, the resonating elements were surrounded by a plenty of parasitic element to ameliorate the radiation property which increased the complexity of the proposed structure. In Ref. [14], 2×2 dual-band MIMO antenna was presented for 28/38GHz 5G applications. The proposed structure has covered the bands 26.6–29.2 and 36.9–39 GHz. The reported antenna was featured with relatively compact size and sufficient bandwidth. But, the peak gain achieved was just 1.83 dB. Similarly, a low profile dual-band dual-element MIMO antenna with comparatively low size has been reported In Ref. [15]. The single antenna element was a slotted monopole antenna resonating at 27 and 39 GHz with wide bandwidth. Nevertheless, only the ECC and diversity gain were investigated to assess the MIMO competency. Besides, the radiation pattern resulted was not much directive. In Ref. [16], an optically transparent four-port MIMO antenna with dual band property has been suggested. The antenna-element was a slotted microstrip patch antenna operating along two wide bandwidths around 26 and 36 GHz. The MIMO antenna was featuring a small volume of $24 \times 20 \text{ mm}^2$, but the maximum gain reached was comparatively low. The researchers in Ref. [17] proposed a quad-port planar millimeter wave MIMO antenna providing 2 GHz of bandwidth from 24.5 to 26.5 GHz. But, the occupied area $30 \times 43 \text{ mm}^2$ is deemed to be comparatively large. Moreover, a metasurface layer has been used to improve the radiation, which further increased the volume and the complexity of the structure. In Ref. [18], a linear 4×4 MIMO coplanar waveguide T-shaped antenna has been introduced for 5G wideband applications.

A peak gain of 10.6 dB was achieved by the MIMO system, however, a large area of $50.8 \times 12 \text{ mm}^2$ has been exploited. Furthermore, the ECC was solely studied. In another related work [19], 4-element MIMO antenna with a full size of $110 \times 55 \text{ mm}^2$ has been created. The elements exhibited dual band operation at 28/38 GHz with good port-isolation and enhanced gain. But, the proposed structure was limited with its great dimensions. In Ref. [20], a 1×4 hook shape array has been proposed for 28 GHz applications. The array was providing 2.4 GHz of bandwidth and marked with compact dimensions of $26.9 \times 18.5 \text{ mm}^2$. Additionally, despite the achievement of satisfactory gain up to 10.3dB, the capacity supplied by this array antenna is the same as which of the single antenna due to the use of single-feeding port. In Ref. [21], a quad elements dielectric resonator-based substrate integrated waveguide (SIW) MIMO antenna has been designed for mmWave 5G wireless systems with total size of $35 \times 35 \times 4.75 \text{ mm}^3$. The proposed structure assured satisfying bandwidth around 26 and 35 GHz and maximum gain of 9.9dB. However, the overall size was relatively large and the employment of vias has further complicate the structure. Also, the dielectric resonator reduced the compactness of the system.

Given the state of the art discussed above, there is yet a necessity to develop a MIMO antenna which can fulfil at the same time the fundamental requirements regarding the small size, simple geometry, wide bandwidth, good radiation properties, high isolation and strong MIMO performance. Indeed, it is revealed that the majority of the reported designs are either large in size or possess a complex structure. Likewise, some MIMO structures are either limited with their low gain or poor bandwidth. Furthermore, neither of the mentioned works has used decoupling structure which can importantly reduce the mutual coupling without increasing the element-spacing considered as a constraint for the devices with limited space. Taking into account the above limitations, the main aim of this study is the suggestion of a new MIMO antenna design that can perfectly meet the small size and wideband requirements without compromising neither the radiation performance regarding the gain and efficiency nor the mutual interference nor the MIMO diversity performance.

This study presents a full investigation of a highly small 4×4 MIMO antenna resonating at 28/38 GHz with dual wide-bandwidth for 5G wireless devices. The suggested MIMO antenna is marked by a simple planar configuration and miniaturized size than the other reported designs. It consists of four elliptical shape radiating elements each is backed with slotted ground assembled orthogonally on the RTRogers 5880 laminate to reduce the mutual coupling. The proposed design is distinguished from the other ones by involving a new decoupling structure to acquire strong isolation level between elements while keeping a

straightforward layout and quite small structure with a total size of $14 \times 14 \times 0.8 \text{ mm}^3$, where the MIMO antenna can be easily incorporated into portable devices. Which constitutes the novelty and the main contribution of this research. In addition, the proposed structure maintains a desired radiation performance including the high radiation efficiency to assure a minimum loss, the good gain, and the directive pattern. Furthermore, the essential parameters of the MIMO antenna including the Envelope Correlation Coefficient (ECC), Diversity Gain (DG), Total Active Reflection Coefficient (TARC), Channel Capacity Loss (CCL) and Channel Capacity (CC) are fully examined to evaluate the MIMO competency. The achieved outcomes proved that the suggested MIMO antenna can act as an excellent candidate for the 5G mmWave wireless communication systems.

This section enables the readers to be familiar with the 5G technology along with the relevant state of the art. The remainder of this research is structured in the following manner. Section 2, is devoted to present a detailed study of the single antenna design including the evolution procedure, the operation principle and the parametrical analysis. Section 3, presents the MIMO antenna configuration and investigates its main achievements including the impedance and radiation properties. In addition, discussions have taken place on the evolvement steps of the MIMO antenna structure and MIMO diversity performance. A comparison with the other existing literature has been exposed in Sect. 4. Finally, Sect. 5 summarizes the research work.

2 Single antenna design

2.1 Antenna configuration

The configuration of the proposed mmWave antenna is depicted in Fig. 1. As can be seen, the antenna structure is made up of an elliptical radiating element of major-radius A and minor-radius B , excited by a 50Ω inset-feed microstrip line of width W_f and length L_f , while a rectangular-slot ground plane is used to back the structure. Considering its low electrical loss, a 0.8 mm Thick RT 5880 Rogers laminate with dielectric constant ϵ_r of 2.2 and tangent loss $\tan \delta$ of 0.0009 is chosen to build the antenna, while the ground plane as well as the radiating element are made up of 0.035 mm thick copper. The overall design was carefully developed, simulated and optimized using the commercially available CST microwave studio simulator, where all the parameters have been neatly optimized to extract the better matched version of the frequency response at both the desired bands. The final parameters dimensions are saved in Table 1. It is worth mentioning that the designed antenna is distinguished by a quite simple geometry and tiny

Fig. 1 Layout of the proposed antenna

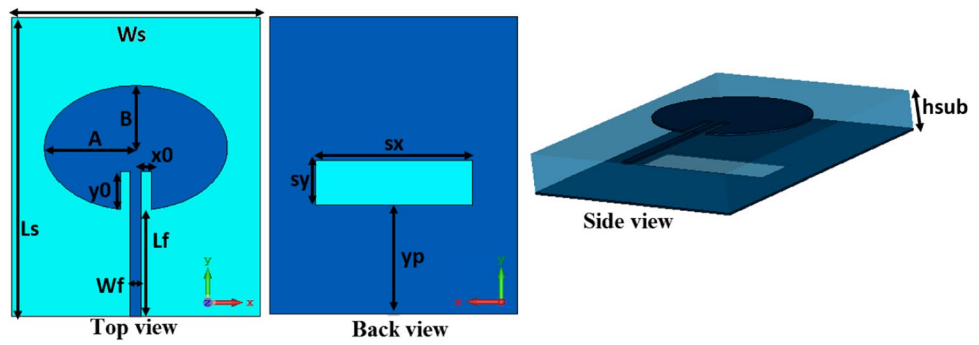


Table 1 Antenna parameters dimensions

Parameter	Value (mm)	Parameter	Value (mm)
Ws	5	y0	0.75
Ls	6	Lf	2.14
hsub	0.8	Wf	0.22
A	1.84	sx	3.18
B	1.25	sy	0.6
x0	0.2	yp	2.2

dimensions of $5 \times 6 \times 0.8 \text{ mm}^3$ which makes it highly suitable for the integration into the 5G wireless equipments.

2.2 Antenna evolution procedure

In order to well comprehend the operating mechanism of the suggested antenna, Fig. 2 displays the progressive modifications through which the suggested design got its resonance in the desired frequency bands at 28 and 38 GHz. As described, the intended antenna is the adjusted version of the conventional Elliptical Microstrip Patch Antenna (EMPA) acquired after three primary stages, where the reflection coefficient at each stage is plotted in Fig. 3. As depicted in Fig. 3a, in the first step, a basic EMPA (Antenna 1) with full ground plane has been chosen as a reference antenna due to the benefits provided such the wider

bandwidth and smaller dimensions at a certain frequency compared to the familiar circular and square patch antennas. The antenna has a total area of $0.55\lambda \times 0.66\lambda \times 0.08\lambda$ ($5 \text{ mm} \times 6 \text{ mm} \times 0.8 \text{ mm}$) where λ is the wavelength at its fundamental resonating frequency.

Initially, the resonant frequency was estimated based on the approximated Mathieu functions (1)-(4) cited below [22], Where A_{eff} is the effective semimajor axis, $f_{11}^{e,o}$ is dual resonant frequency of the dominant odd and even modes,

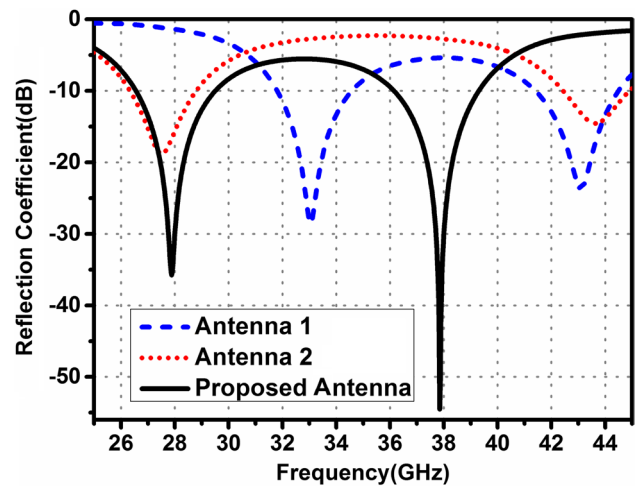
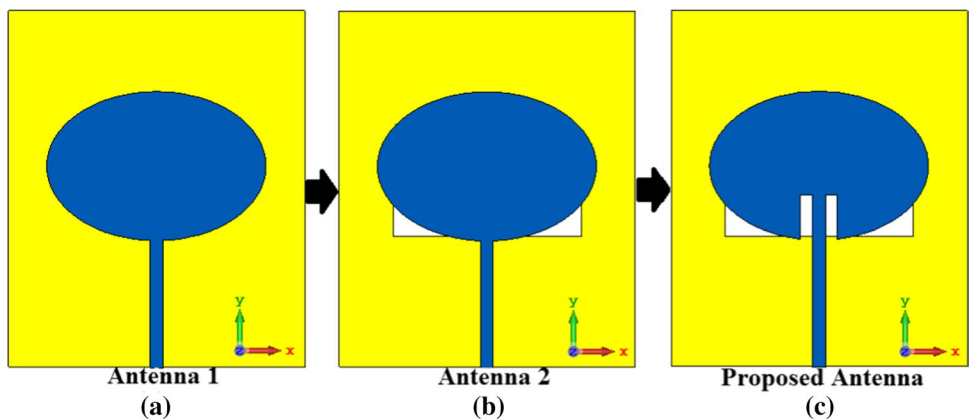


Fig. 3 Reflection coefficient of the stepwise geometries

Fig. 2 Step-by-step geometric evolution of the suggested antenna



$q_{11}^{e,o}$ is approximated Mathieu function for the dominant mode $TM_{11}^{e,o}$ and e is ellipse eccentricity. Whereas, the resonant frequency has been wisely adjusted by optimizing the overall antenna dimensions using the computational software CST studio.

As plotted in Fig. 3, the reference antenna (Antenna 1) generates its first resonance with reasonable bandwidth at approximately 33 GHz and the range of frequency was extended farther beyond 33 GHz during simulation to detect its next higher-order resonance. Indeed, it

$$A_{eff} = A \left[1 + \frac{2h_{sub}}{\pi\epsilon_r A} \left\{ \ln \left(\frac{A}{2h_{sub}} \right) + (1.41\epsilon_r + 1.77) + \frac{h_{sub}}{A} (0.268\epsilon_r + 1.65) \right\} \right]^{1/2} \tag{1}$$

$$f_{11}^{e,o} = \frac{15}{\pi e A_{eff}} \sqrt{\frac{q_{11}^{e,o}}{\epsilon_r}} \tag{2}$$

$$q_{11}^e = -0.0049e + 3.7888e^2 - 0.7278e^3 + 2.314e^4 \tag{3}$$

$$q_{11}^o = -0.0063e + 3.8316e^2 - 1.1351e^3 + 5.2229e^4 \tag{4}$$

is found out that the antenna excites a second higher-order resonance around 43 GHz besides its fundamental resonance. Thus, the first antenna supports two distinct resonating modes which can be identified by the current density, illustrated in Fig. 4a, b. As shown in Fig. 4a, at the fundamental resonance 33 GHz the current passes over the transmission line and disperses uniformly across the elliptical patch while the maximum intensity is mainly concentrated over the patch-edge. Additionally,

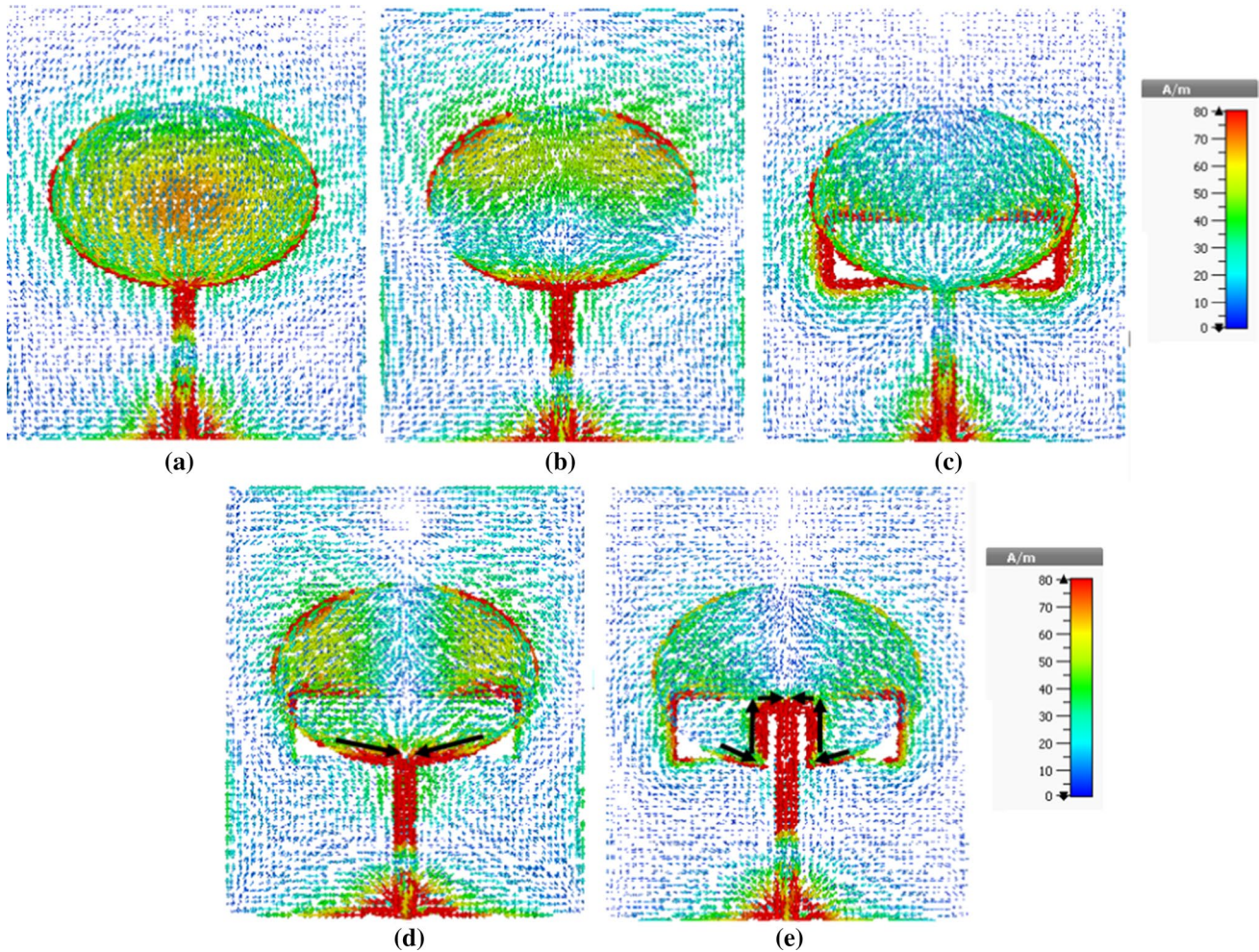


Fig. 4 Surface current density of **a** Antenna 1 at 33 GHz. **b** Antenna 1 at 43 GHz. **c** Antenna 2 at 28 GHz. **d** Antenna 2 at 43.5 GHz. **e** Proposed antenna at 38 GHz

the electrical current spread out continuously along the ground plane while it is getting more intense beneath the radiating element which is attributed to the strong electromagnetic coupling with the resonant elliptical patch. In contrast, according to the Fig. 4b, a lower current intensity is remarked over the ground at the higher resonant frequency 43 GHz which points to a less coupling effect with the resonant patch, while the current density is principally intensified on the patch extremity especially in the bottom edge of the elliptical patch where the transmission line is connected. However, although the reference antenna provides a wide band property at both resonant frequencies, the target frequency bands are not attained and geometrical modifications are required to tune the two resonance frequencies at the desired bands.

Accordingly, the second step (Antenna 2) is performed with the target of adjusting the first resonance at the desired frequency, specifically 28 GHz. This purpose is reached by using defected ground structure (DGS), where a rectangular slot is engraved on the ground straightway under the resonant patch as presented in Fig. 2b. Indeed DGS technology has been widely used owing to its easiness in implementation and its effectiveness to improve and amend the antenna performance. Generally, the defect may have a periodic or non-periodic structure which is engraved either beneath or on the sides of the radiating element. The inclusion of the defects at the level of the ground plane changes the effective capacitance and inductance of the antenna which may generate various responses according to the position, geometry and periodicity of the defect. It can be employed for band rejection, multiband operation, bandwidth enlargement, miniaturization and impedance matching refinement... etc. While in this paper the DGS has been used for frequency amendment. As plotted in Fig. 3, after embedding the slot in the finite ground plane a new configuration is acquired (Antenna 2) where the fundamental resonance has shifted from 33 GHz towards the lower frequencies, settling around 28 GHz by carefully tuning the slot size and placement. Meanwhile, the upper resonant frequency is slightly shifted to the higher frequency side, indicating that the etched slot affects principally the first resonating frequency.

The surface current flow of Antenna 2 at 28 GHz is depicted in Fig. 4c. As displayed, loading the rectangular slot on the ground plane led to distort its uniformity and create a local loss of conductivity which perturbed the electric current circulation and broken its continuity. Indeed, the inserted slot forced the current to flow intensively around its extremities, dramatically changing the current path along the ground. This alteration of electric current distribution has obviously affected the antenna characteristics leading in turn to shift the lower resonant frequency of the conventional

antenna (Antenna 1) towards the intended band around 28 GHz.

Similarly, the final step is implemented with the intention to bring the upper resonant frequency of Antenna 2 to the second desired frequency band, namely 38 GHz. To achieve that purpose, extending electric current path on the radiating element at the frequency to be amended is an effective technique. As presented in Fig. 4d, at the upper resonance 43.5 GHz of Antenna 2, the maximum current intensity is transmitted through the feed line and condenses exactly around the lower-edge linking the elliptical patch with the latter. Therefore, in order to stretch the electric current circulation at this frequency, a pair of notches has been inserted in the radiation patch on the left and right side of the feeding line as displayed in Fig. 2c, which converts the excitation technique from an edge feed line to an inset-feed line, so the proposed antenna is finally attained. As expected, Fig. 3 reveals that the inclusion of the inset-feed notches does efficiently result in the switching of the upper resonance of Antenna 2 from 43.5 GHz to the targeted frequency band at 38 GHz. According to the surface current distribution depicted in Fig. 4e, the shift of the second resonant frequency is ascribed to the electric current path expansion. Indeed, the added notches served to offer an extra path (extra edges) for the current flow, which led to artificially enlarge the electric length of the antenna at the upper resonance. Which is responsible to reduce the latter smoothly from 43.5 GHz to 38 GHz. Furthermore, the employment of inset-feed technique with the fine refinement of its width x_0 and length y_0 contributed to achieve the best impedance matching with bandwidth enhancement for both resonating frequencies. Consequently, the combination of DGS and inset-feed technique has successfully contributed to adapt the resonance frequencies of the suggested antenna at the desired frequency bands without requiring to increase the antenna dimensions, which kept a miniaturized structure. The reflection coefficient of the final optimized antenna was carried out using both CST and High Frequency Structure Simulator (HFSS) for comparison purpose. As plotted in Fig. 5a, the S11 curves extracted from both computational tools are in very good coherence which indicated the validity of the design. Accordingly, it is noted that the proposed antenna operates at two prominent frequency bands, resonating at 28 and 38 GHz with low reflection coefficient of -35 dB and -52 dB respectively. A wideband property of approximately 3 GHz has been noted at both resonance, where the first band starts from 26.5 to 29.5 GHz while the second band starts from 36.15 to 39.3 GHz.

The antenna input impedance Z_{in} can be expressed as a complex number where the real part is the antenna resistance (R_{in}) and the imaginary part is the antenna reactance (X_{in}). To achieve a good impedance matching at a given frequency

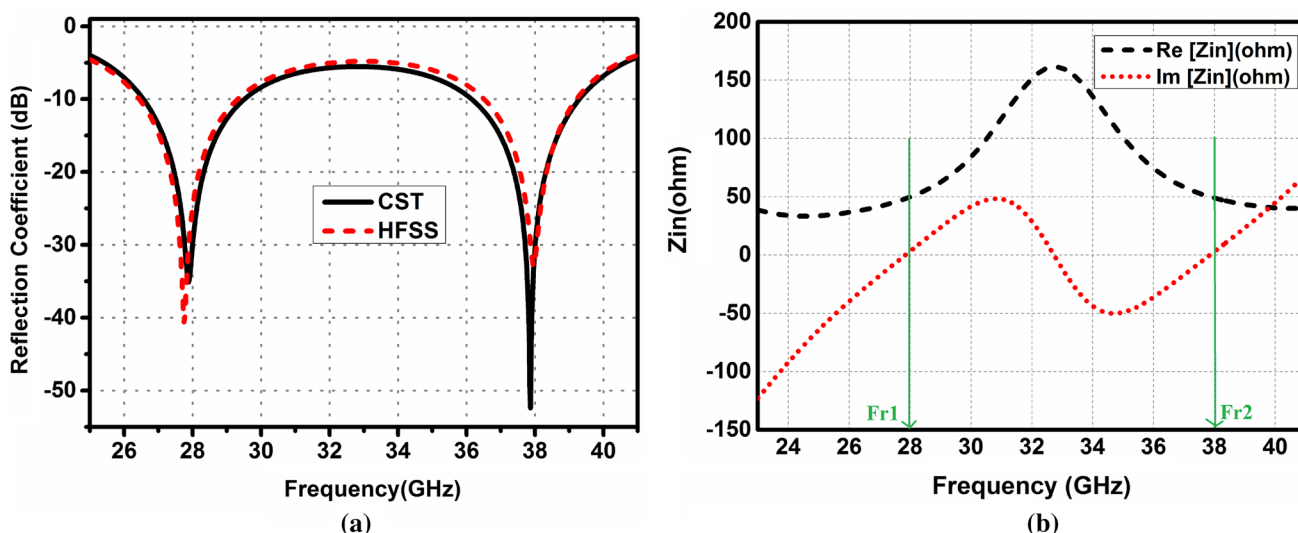


Fig. 5 Impedance characteristics of the proposed antenna **a** Reflection coefficient S11. **b** Input Impedance Zin

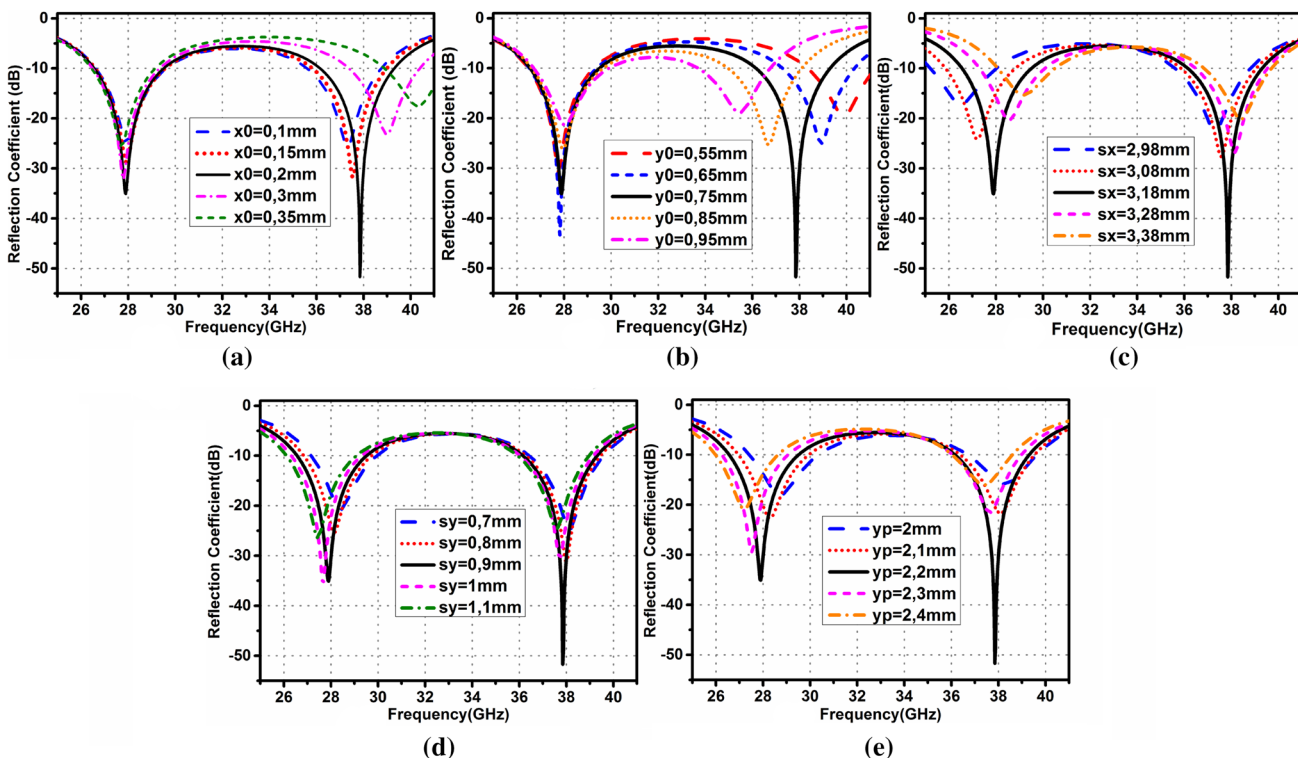


Fig. 6 Parametrical study on the reflection coefficient by varying different parameters **a** x_0 . **b** y_0 . **c** s_x . **d** s_y . **e** y_p

the input impedance should be close to 50Ω , meaning that the resistance should be close to 50Ω and the reactance should be close to 0Ω . The input impedance of the proposed antenna is shown in Fig. 5b, as seen, the {resistance,

reactance} of the antenna at the resonance frequencies 28 and 38 GHz are approximately found to be $\{49.5 \Omega, 0.88 \Omega\}$ and $\{48.8 \Omega, -0.11 \Omega\}$ respectively. Which presents a very good matching.

2.3 Parametrical analysis

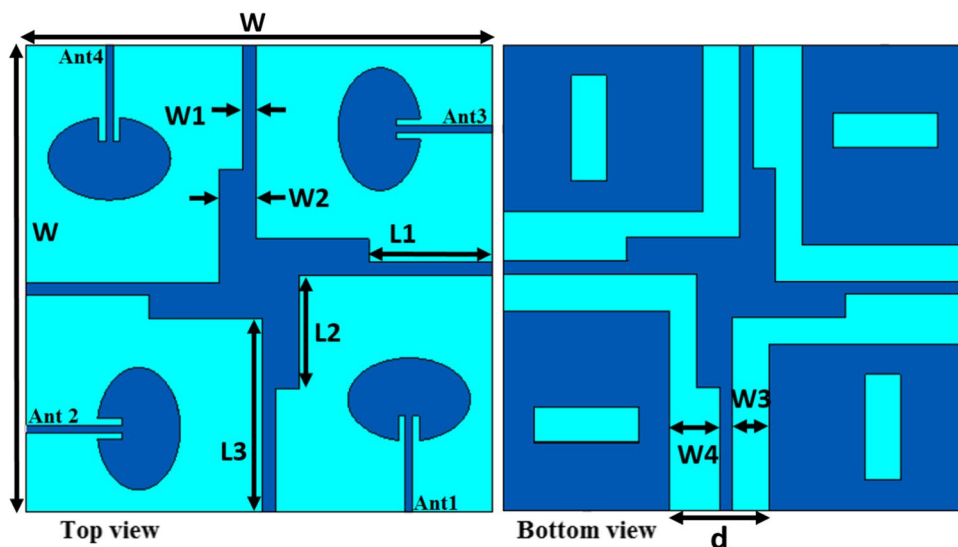
The parametric study is an inevitable step in antenna designing. It serves to find the optimized parameters allowing the extraction of the best antenna performance. In this work, one of the intended outcomes is the adjustment of the antenna resonance precisely at 28 and 38 GHz. For that, a detailed study has been carried out to well know the effect of the parameters related to the inset-feed and the slot on the reflection coefficient behavior. The effect of the width x_0 and length y_0 of the inset-feed are plotted in Fig. 6a, b respectively, while the effect of the width s_x , length s_y and position y_p of the slot in the ground are illustrated in Fig. 6c–e. During the parametric analysis, when a parameter is changed the others are kept unchanged. As observed in Fig. 6a, by switching the inset-feed width x_0 from 0.1 to 0.35 mm, the second resonance frequency is swiped right from 37 GHz to 40.2 GHz. Where the resonance at the desired frequency is reached with the best impedance matching at $x_0 = 0.2$ mm. Similarly, as illustrated in Fig. 6b, when the inset-feed length y_0 increased from 0.55 to 0.95 mm, the second resonating frequency decreased from 40 GHz to 35.5 GHz. While, at the optimal length of 0.75 mm, the resonance is occurred at the required frequency of 38 GHz with the lowest reflection coefficient of -52dB. It is noticed that the inset-feed parameters have a significant effect on the upper resonance frequency. Whereas, the lower resonance at 28 GHz kept stable. In contrast, a considerable effect on the latter is noted when varying the slot parameters. As can be seen in Fig. 6c, the increase of the slot width s_x from 2.98 to 3.38 mm led to shift right the first resonance from 26.5 to 29 GHz while the second resonance is swiped from 37.2 to 38.5 GHz. Where, the intended resonance frequencies are attained at the optimum width s_x of 3.18 mm. The impact of the slot length s_y on the reflection coefficient is plotted in Fig. 6d. As presented, both resonating frequencies show less sensitivity when the slot width is varied from 0.7 to 1.1 mm. However, it is revealed that the fine-tuned resonant frequencies are got only when the length s_y has the optimum value of 0.9 mm. A parametrical study has been also carried out on the influence of the slot position y_p on the antenna response. As clearly remarked, by swapping the slot position from 2 to 2.4 mm, both resonant frequencies are slightly switched left from 28.8 GHz to 27.2 GHz and from 38.5 GHz to 37.5 GHz respectively. Moreover, a profound degradation of the impedance matching is noted at the second resonance, where the optimized response is detected when the value of y_p is 2.2 mm. Thus, the performed parametrical study has proven that the width y_0 and length x_0 of the inset-feed notches as well as the slot width s_x , the slot length s_y and the slot position y_p are all a key parameters to effectively control the antenna resonating frequencies, the impedance matching and the operating bandwidth.

This section allowed us to be aware of the single antenna design and its operation mechanism. It should be stressed that the suggested design assemblies the most in-demand traits including the multi-wideband operation, the simple planar geometry and the miniaturized structure. These features are highly required in the futuristic wireless devices targeting the millimeter wave 5G communications, which will undoubtedly integrate the antennas in MIMO structures for the high data rate purpose. Accordingly, the next section has been allocated to assess the performance of the MIMO antenna constructed relying on the single antenna unit.

3 MIMO antenna design

The MIMO is deemed an indispensable technology in the implementation of the 5G systems to reach the sought-after capacity and throughput without exhausting the bandwidth and transmitted power. However, designing any MIMO system raises two main challenges which are the small size to accommodate the narrow space in portable equipments and the fulfillment of high isolation level to decrease the mutual coupling between the MIMO-element along the desirable band. In a MIMO system, the mutual coupling generally presents the amount of energy coupled to a close antenna when an antenna is powered. It may severely affect the antenna characteristics such as the radiation, the reflection coefficient, the input impedance and the diversity performance if not carefully weakened [23]. To surpass these issues, many decoupling methods have been discussed and researched which can be classified into three types. The first type includes decoupling schemes based on spatial and polarization diversities, where the spatial diversity can be implemented by placing the antenna-element with large spacing which is not practical. Whilst, polarization diversity can be realized by vertically positioning the antenna elements to create orthogonal polarization as a mean to generate uncorrelated channel. Generally, polarization diversity is most desirable because the elements can be placed closely to one other. However, the mutual coupling becomes difficult to handle when more than two elements is used. The second decoupling type involves introducing decoupling structure to suppress or block the coupling among elements, which can be made using various techniques such as DGS, electromagnetic band gap (EBG), metamaterial based structure, neutralization line, shorting pin and parasitic structures, ...etc. [23]. The last type is hybrid and leading to a high decoupling level, it results from combining the two former types involving diversity techniques and decoupling structure, which is adopted in this work.

Fig. 7 Top and bottom view of the proposed MIMO antenna model



3.1 Layout of the MIMO antenna and S-parameters

The Layout of the proposed MIMO antenna is displayed in Fig. 7. As depicted, a 4×4 MIMO antenna is constructed by orthogonally arranging four units of the single antenna on the same RTRogers 5880 substrate with spacing d of 3 mm and a full size of $14 \times 14 \times 0.8 \text{ mm}^3$. The vertical placement results in polarization diversity giving rise to isolation enhancement. Subsequently, a cross shaped isolator is centered between elements in the front and rear side to bring better isolation improvement. The MIMO antenna design and the decoupling structure are developed and neatly optimized using CST software. The final geometrical parameters dimensions are listed as following: $W = 14 \text{ mm}$, $W1 = 0.4 \text{ mm}$, $W2 = 1.1 \text{ mm}$, $W3 = 1.1 \text{ mm}$, $W4 = 1.5 \text{ mm}$, $L1 = 3.7 \text{ mm}$, $L2 = 3.4 \text{ mm}$, $L3 = 5.8 \text{ mm}$ and $d = 3 \text{ mm}$.

It should be mentioned that during the simulations, when an element is excited the three others are terminated with 50Ω matched loads. The reflection coefficients and transmission coefficients (mutual coupling) among elements of the suggested MIMO structure are plotted in Fig. 8. As clearly seen, all elements show a similar reflection coefficient with good performance due to the symmetry and similarity of the elements. The four elements resonate exactly at 28 and 38 GHz with a desirable bandwidth of 3 GHz (26.62–29.71 GHz) and 3.2 GHz (36.3–39.5 GHz) respectively. Furthermore, the worst case mutual coupling noted between ports is below -30 dB along both operating bands which proves a very high isolated MIMO elements. The progressive stages to build the decoupling cross structure for better isolation are described in the next subsection.

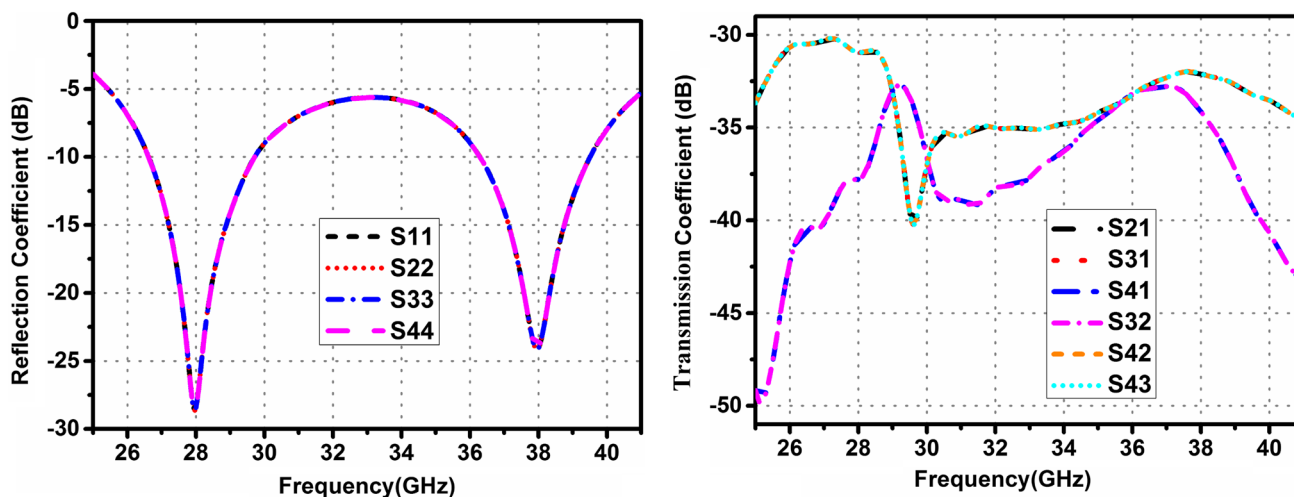
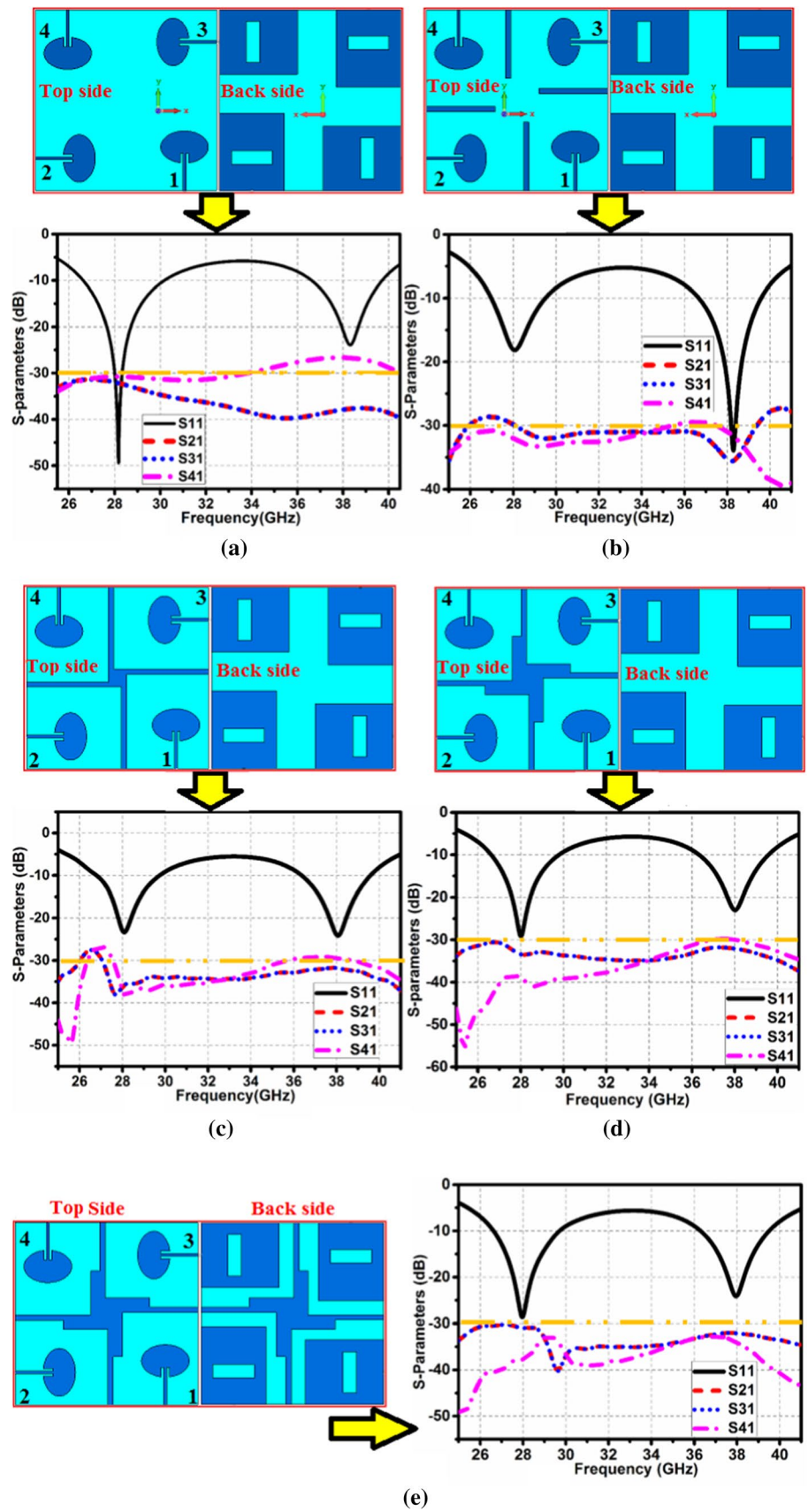


Fig. 8 Reflection coefficient and transmission coefficient of the proposed MIMO antenna

Fig. 9 Evolution steps of the proposed decoupling structure attached with their corresponding S-parameters **a** Step-1. **b** Step-2. **c** Step-3. **d** Step-4. **e** Step-5



3.2 Evolution process of the decoupling structure

This subsection is allocated to analyse the evolution mechanism followed to reach the isolation structure allowing an optimized decoupling between all the excitation ports, which is carefully presented in Fig. 9, where each step is accompanied with its own S-parameters. Given the similarity and the symmetrical arrangement of the MIMO elements, only the S-parameters related to the first element (S11, S21, S31, and S41) are considered for analysing the decoupling evolution process out of the sixteen S-parameters of the four-port MIMO antenna. As manifested in Fig. 9a, in the initial step taken as reference, the design was started without any isolation structure while the MIMO elements are arranged orthogonal to each other. The reflection coefficient plot of this initial configuration shows a good bandwidth feature and maintains a good impedance matching in both bands while a slight shift has occurred in both resonant frequencies from 28 to 28.2 GHz and from 38 GHz to 38.4 as compared to the single antenna which is referred to the variation in the substrate dimensions and the interaction between the MIMO elements. More important, the mutual coupling of adjacent elements (S21 & S31) reports high decoupling above 30dB in both bands while the transmission coefficient of diagonal elements S41 shows a minimum decoupling up to 26dB along the higher band specially which can be further increased to boost the MIMO performance. Hence, the next steps are executed with the intention to reduce the interference among diagonal elements using an effective isolating structure. As seen in Fig. 9b, in the second step, the isolation enhancement is proceeded with four identical simple metallic stubs printed between the adjacent elements on the top substrate's layer where the stubs length of 5.3 mm is near to the guided wavelength $\lambda_g = \frac{c}{f\sqrt{\epsilon_r}}$ at 38 GHz where the corresponding S-parameters is plotted in the same Fig. 9b. As manifested, the application of the metallic stubs, acting as reflectors, has contributed to reduce the electromagnetic energy coupled to the diagonal units leading to decrease the mutual coupling S41 from -26.5 dB to below -29.5 dB in the higher band. Nevertheless, the isolating stubs have badly interacted with the elements in the lower band, where the impedance matching at the lower resonant frequency is disturbed conducting to regress the reflection coefficient to less than -20 dB and the bandwidth is decreased by 1 GHz from 3.5 GHz (30.1–26.6 GHz) to 2.5 (26.9–29.4 GHz). In addition, the isolation amongst adjacent elements have relatively decreased. Hence, further modifications are required to maintain the improved mutual coupling (S41) and getting back the enhanced S-parameters in the lower band. Accordingly, in

the third step shown in Fig. 9c, the isolating stubs have been united at the centre of the substrate so the separated stubs have been converted to a cross-shaped structure. As demonstrated by the corresponding S-parameters, the novel structure helped to ameliorate the impedance matching in the lower band resulting in low reflection coefficient up to -24 dB and enhanced bandwidth up to 2.94 GHz (26.8–29.7 GHz). Moreover both resonating frequencies has been exactly tuned at 28/38 GHz. However, the inter-element mutual coupling has been disturbed and shifted toward the lower values where a maximum value up to -26.5 dB is reached.

Next, in the fourth step revealed in Fig. 9d, the decoupling cross has been reinforced by adding four additional stubs of length 3.4 mm meet at the structure's center, resulting in obtaining the suggested isolating structure. Whereas, the extra metallic strips length is approximately $0.5\lambda_g$ and $0.6\lambda_g$ at 28/38 GHz respectively. Hence, the new structure served to further optimize the reflection coefficient to below -29 dB at the lower resonance, besides restoring the isolation of adjacent elements to above 30dB in the whole band and convincingly improve the isolation among diagonal elements to approx. 40dB in the lower band while it settled at a minimum of 29.7 dB in the 38 GHz band. The final step exhibited in Fig. 9e, is carried out by reproducing the suggested decoupling cross structure in the bottom substrate's layer between the ground planes where the procured S-parameters clearly manifest that the occurred replication works to strengthen the isolation of diagonal elements to more than 32.5 dB throughout the entire band and assuring a maximum isolation of 40dB in both operating bandwidths besides keeping a high isolation within the range of 30–40dB between adjacent elements. Furthermore, it is noticed that the proposed structure does not affect negatively the antenna frequency response where the reflection coefficient kept a wide bandwidth property reaches to 3.1 GHz (26.62–29.71) and 3.2 GHz (36.3–39.5 GHz) with good impedance matching at the respective bands 28/38 GHz. Consequently, it can be concluded that the proposed structure is succeeded to considerably weak the direct mutual coupling among elements where further explanation on its effectiveness to absorb the coupling fields is discussed in the next subsection.

3.3 Stepwise evolution of the mutual coupling reduction

In an effort to well known the effectiveness of the proposed structure to ensure a low mutual coupling, Fig. 10 presents the mutual coupling of the three stepwise geometries through which the proposed MIMO antenna design has been attained. It must be emphasized that the spacing d between the separated ground planes is fixed at 3 mm during all evolution

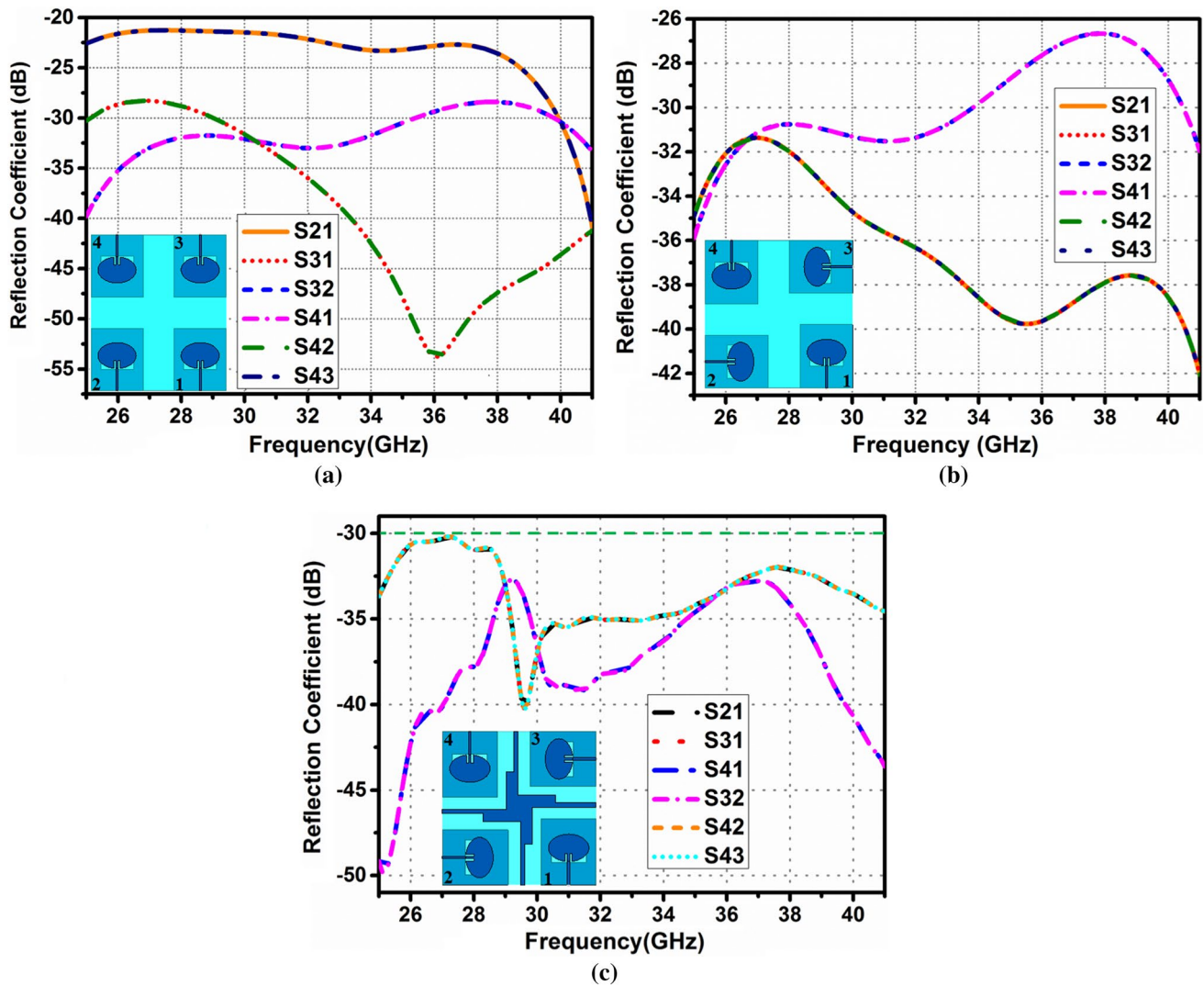


Fig. 10 Mutual coupling behavior of the three progressive MIMO structures **a** Parallel arrangement. **b** Orthogonal arrangement. **c** Orthogonal arrangement with decoupling structure (proposed)

steps. A preliminary configuration of the MIMO antenna without isolation structure and polarization diversity has been produced as can be seen in the inset-image of Fig. 10a, where all element pair allows spatial diversity. This reference layout provides a minimal isolation of 21 dB detected between the contiguous elements (1, 2) and (3, 4) and a minimum isolation more than 27.5 dB is reached between non adjacent elements (1, 3), (1, 4), (2, 3) and (2, 4). In order to better improve the port-isolation between the neighboring antennas without extending the elements spacing d , a new plan has been followed. In this plan, the second and third elements are rotated with 90° clockwise as seen in the inset-image of Fig. 10b. So, a new configuration is obtained where each two successive elements are orthogonal to each other. This arrangement serves to achieve orthogonal polarization recognized as polarization diversity to weaken the mutual

coupling among orthogonal elements. As displayed in Fig. 10b, with this new arrangement, the minimal isolation between perpendicularly adjacent elements is exceeding 30 dB, where the amount of isolation improvement is more than 10 dB as compared to the isolation among adjacent components in the first structure. Indeed, the mutual coupling mitigation is occurred due to the cross polarized direction of the electric field vectors (orthogonal orientation of the E-field vectors) produced by the orthogonal elements, leading to generate non-overlapping E-field. Hence, less coupling energy is induced between each other. In contrary, no isolation improvement is noted between non-orthogonal elements (1, 4) and (2, 3) as they don't provide orthogonal polarization.

The strength of polarization diversity to guarantee high isolated elements can be further demonstrated by

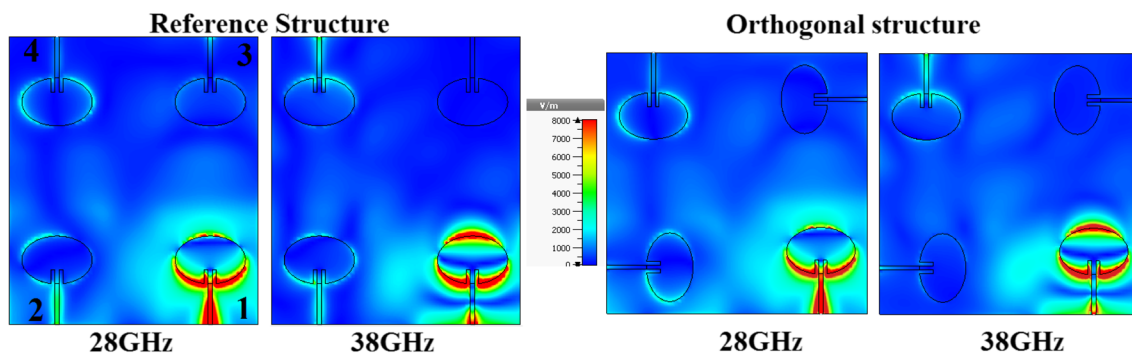


Fig. 11 E-Field distribution on the Reference and Orthogonal MIMO antenna structures at the resonant frequencies 28/38 GHz

observing the E-field distribution on the MIMO antenna with and without orthogonal placement at both resonating frequencies, displayed in Fig. 11. Here, the first element (port 1) is powered and the others are defined with 50 Ω matched loads. As we can clearly see, when the first element of the reference MIMO configuration is energized, an E-field amount with remarkable intensity is spread through the substrate and coupled into the other elements especially elements 2 and 4 at both resonant frequencies.

By using the orthogonal configuration, the electric field coupling amount is considerably minimized specially between the elements enabling polarization diversity, i.e. (1, 2) and (1, 3) which explains the weak mutual coupling (< -30 dB) achieved among them over the whole frequency range. However, no decoupling enhancement is noted between the diagonally placed elements (1, 4), where the coupling field within the fourth element remains unchanged for both structures. Which is self-evident as both elements still have the same plane of polarization.

Accordingly, as shown in the inset image of Fig. 10c, a cross-shaped decoupling structure has been carefully developed, optimized and placed in the top and bottom layers of the substrate with the aim to engender further decoupling between diagonal elements. As expected, the mutual coupling plotted in Fig. 10c shows that the application of the isolating structure degrades significantly the coupling especially between diagonal elements

(1, 4) and (2, 3), where the mutual coupling is decreased by 7 dB from -26.5 dB to -32.5 dB in the second bandwidth and settled below -32.5 dB in the whole frequency range. To further expound the effect of the cross-shaped isolator on the isolation performance, Fig. 12 presents the E-field distribution before and after inserting the decoupling structure. As can be clearly remarked, the application of the cross shaped isolator plays a key role to block the propagation of the E-field generated from the first element and restrict its coupling into the other elements, where most of the coupling field is focused around the decoupling cross, which inherently resulted in mutual coupling minimization. As a result, the suggested MIMO antenna is marked by excellent isolation exceeding 30 dB and 32.5 dB between orthogonal elements and diagonal elements respectively which certainly meets industrial requirement.

3.4 Radiation characteristics

The 2D far-field radiation pattern (gain value) of the proposed MIMO antenna has been observed in the two cutting planes $\varphi=0^\circ$ (xoz) and $\varphi=90^\circ$ (yoz) at 28 and 38 GHz for the two orthogonal elements (1, 2) denoted as Ant 1 and Ant 2 respectively. As displayed in Fig. 13, at both frequencies 28/38 GHz, the antenna elements are distinguished by highly directive, stable and focused far-field patterns in both planes xoz and yoz. Where, the main lobe radiation is always oriented towards the

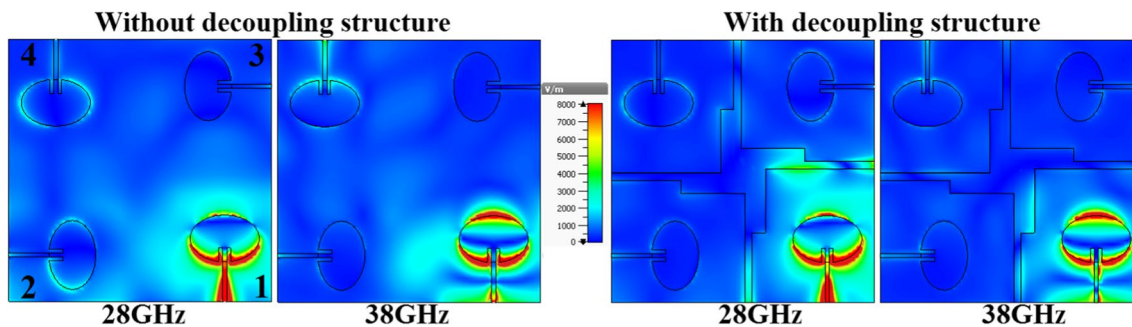


Fig. 12 E-Field distribution on the orthogonal MIMO antenna with and without decoupling structures at both resonant frequencies 28/38 GHz

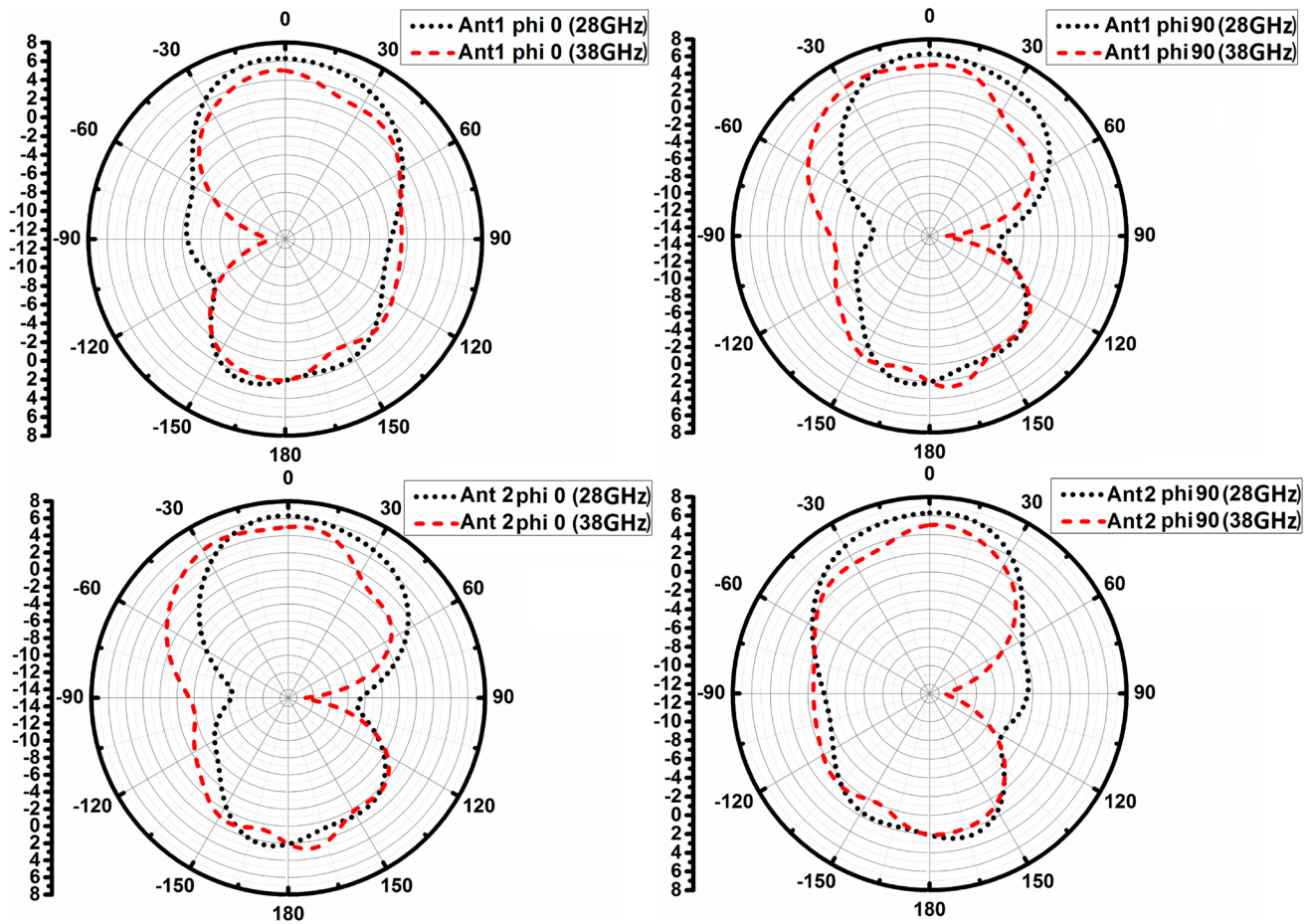


Fig. 13 Two-dimensional radiation patterns of the elements 1 and 2 at both resonating frequencies 28/38 GHz in the principal cutting planes xoz ($\phi=0^\circ$) and yoz ($\phi=90^\circ$)

broadside direction around $\theta=0^\circ$, which is a required feature in mm-wave communications for efficacious transmission-reception ability. Additionally, it is reported that the radiation patterns of Antenna 1 and Antenna 2 in xz -plane ($\phi=0^\circ$) are totally reversed in yz -plane ($\phi=90^\circ$) for both frequencies. In another word, the H-plane (xoz) and E-plane (yoz) of Antenna 1 are found in reverse order for Antenna 2, which validates the phenomenon of polarization diversity and confirms that the elements have different polarization planes.

Furthermore, the simulated 3D far-field radiation patterns for all elements at both resonant frequencies are shown in Fig. 14. As displayed, the antenna elements maintain a stable radiation patterns performance not degenerated by the MIMO configuration, which indicate the independency of elements in their individual performance. Also, it is noted that the 3D patterns of the orthogonal elements are rotated by 90° from each other, which may be helpful to provide uncorrelated patterns, desirable to mitigate the multi path effect occurred in communication systems. Next, in order to verify the other radiation characteristics of the MIMO antenna, radiation efficiency and peak gain across the two operating bandwidths are revealed in Fig. 15. A high

radiation efficiency exceeding 98% is noticed in both bands by virtue of the low-loss substrate used, where the efficiency attained at 28 and 38 GHz is 98.8% and 98.5% respectively. Besides, a good gain characteristic is noted with a maximum value up to 6.8dB achieved in the first band. While, a peak gain of 6.33dB and 5dB is reached at the lower and upper resonance frequencies respectively. Hence, the radiation characteristics achieved emphasize the practicability and suitability of the inserted decoupling structure as it does not degrade the radiation performance which is considered an essential requirement.

3.5 Diversity performance analysis

The diversity performance of the suggested MIMO antenna is assessed by investigating the essential metrics represented by Envelop Correlation Coefficient (ECC), Diversity Gain (DG), Total Active Reflection Coefficient (TARC), Channel Capacity Loss (CCL) and Channel Capacity (CC). The ECC is considered one of the most critical diversity parameters to examine in MIMO antenna designing. It measures the correlation level achieved between the radiation patterns of the different MIMO

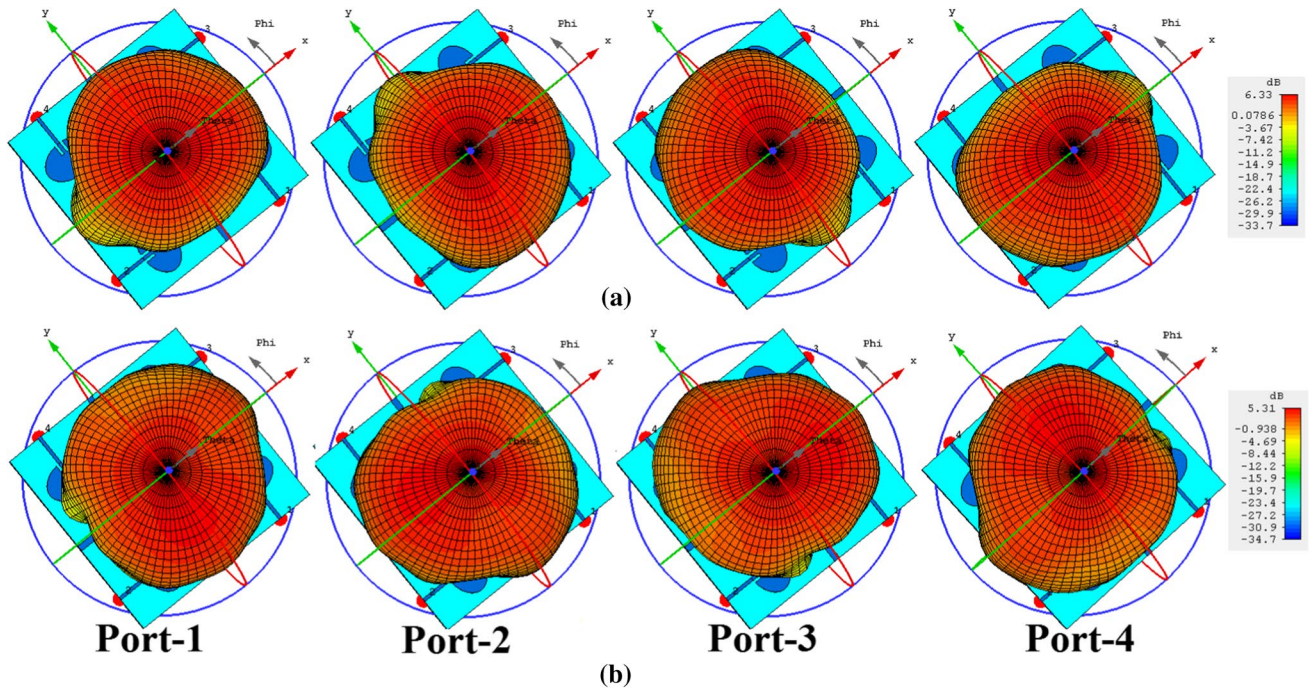


Fig. 14 Three-dimensional radiation patterns of the 4-element MIMO antenna at a 28 GHz. b 38 GHz

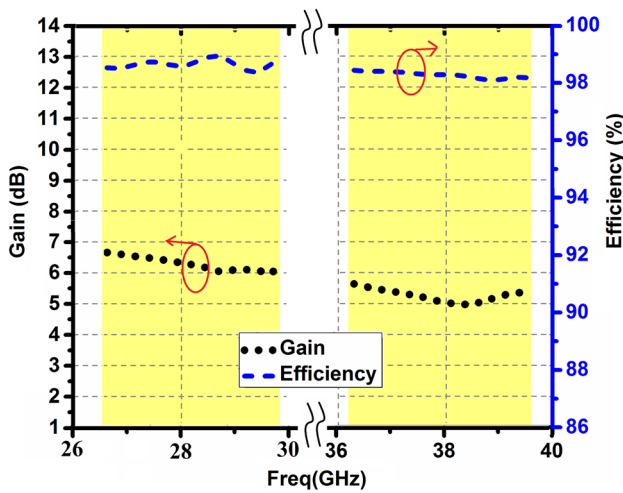


Fig. 15 Radiation efficiency and gain versus frequency of the proposed MIMO antenna

elements when they are simultaneously excited [1, 8, 24]. In the ideal case, the ECC should be zero which produces a MIMO elements perfectly decoupled where the elements radiation patterns do not affect each other. Hence, in order to assure a MIMO system with high pattern diversity a low correlation should be attained and should not exceed the practical limit fixed at 0.5 for any application. The ECC is calculated between MIMO antenna elements using Eq. (5) relying on S_{ij} parameters where S_{ii} , S_{jj} denote the reflection coefficients of the i^{th} , j^{th} elements respectively and S_{ij} denotes the mutual coupling between the

i^{th} , j^{th} antennas. As depicted in Fig. 16a, the calculated ECC between any two elements is less than 0.0005 and 0.00025 across the two operating bandwidths respectively. The obtained values are extremely low than the recognized threshold which grants high diversity performance.

$$ECC_{ij} = \frac{|S_{ii}^* S_{ij} + S_{ji}^* S_{jj}|^2}{\left(1 - (|S_{ii}|^2 + |S_{jj}|^2)\right) \left(1 - (|S_{ij}|^2 + |S_{ji}|^2)\right)} \tag{5}$$

Another crucial parameter to be evaluated is Diversity Gain (DG) which is related to the ECC by Eq. (6). For a MIMO antenna the DG measures the amount of power transmission reduction without occurring performance loss when diversity scheme is employed. In simple terms, in a multipath environment, the DG of a MIMO antenna can be presented as the difference between the signal to noise ratio (SNR) of the combined signals and the SNR of a single antenna in one diversity channel [24]. For a good MIMO performance, the diversity gain should be close to 10dB. As depicted in Fig. 16a, the DG between any two antenna elements is more than 9.99dB over the whole working bandwidths and reach to 10dB at the resonance frequencies which expresses a very good diversity performance.

$$DG_{ij} = 10\sqrt{1 - (ECC_{ij})^2} \tag{6}$$

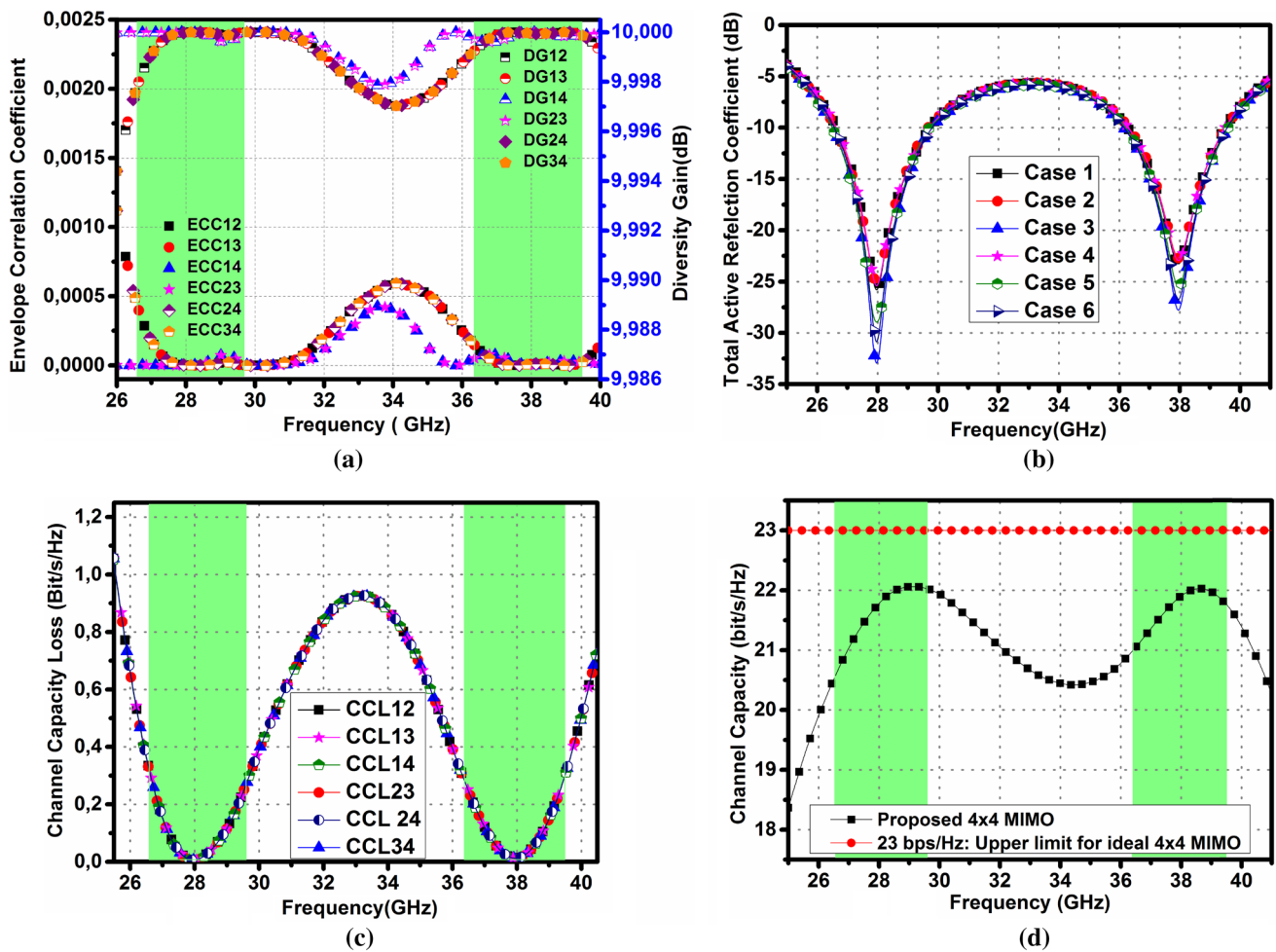


Fig. 16 Performance diversity of the proposed MIMO antenna. a ECC and DG. b TARC. c CCL. d Channel capacity

Another important parameter to be examined is the Total Active Reflection Coefficient abbreviated by TARC. It defines the square root of the ratio of the total reflected power to the total incident power for a MIMO antenna. The TARC has the same meaning of the reflection coefficient for the single antenna [25]. It can be considered as the reflection coefficient of the overall MIMO system and used to determine the effective bandwidth of the MIMO antenna. It is varied between 0 and 1, where 0 value means the incident power is totally radiated while 1 value means the incident power is totally reflected. The TARC calculation relies on several parameters including the mutual coupling, reflection coefficients and excitation phases to consider the random signals summation at each port. It is expressed by Eq. (7), where N is the ports number, a_i and b_i present the incident and reflected power at the i^{th} respectively. The b-vector of the reflected power is calculated using Eq. (8). According to the formula, all ports are excited with signals of equal

amplitude a_1 . Nonetheless, the signal of the first port has a null excitation phase (e^{j0}), whereas different phases from θ_1 to θ_{N-1} are applied to the rest of ports. Here, the combination of phases applied at each port are arbitrary selected between 0° and 180° , while six various cases have been considered as following:

Case 1: $0^\circ; 0^\circ; 30^\circ; 60^\circ$ / Case 2: $0^\circ; 15^\circ; 45^\circ; 75^\circ$ / Case 3: $0^\circ; 30^\circ; 60^\circ; 90^\circ$.

Case 4: $0^\circ; 45^\circ; 75^\circ; 180^\circ$ / Case 5: $0^\circ; 65^\circ; 85^\circ; 120^\circ$ / Case 6: $0^\circ; 35^\circ; 70^\circ; 130^\circ$

$$\Gamma_a^r = \sqrt{\sum_i^N |b_i|^2} / \sqrt{\sum_i^N |a_i|^2} \tag{7}$$

$$b = \begin{bmatrix} b_1 \\ \vdots \\ b_N \end{bmatrix} = \begin{bmatrix} S_{11} & \cdots & S_{1N} \\ \vdots & \ddots & \vdots \\ S_{N1} & \cdots & S_{NN} \end{bmatrix} \begin{bmatrix} a_1 \\ \vdots \\ a_N \end{bmatrix} = \begin{bmatrix} S_{11} & \cdots & S_{1N} \\ \vdots & \ddots & \vdots \\ S_{N1} & \cdots & S_{NN} \end{bmatrix} \begin{bmatrix} a_1 e^{j0} \\ \vdots \\ a_1 e^{j\theta_{N-1}} \end{bmatrix} \tag{8}$$

The TARC of the MIMO antenna is plotted in Fig. 16b. As revealed, for the six-cases, the calculated TARC maintains the original form of the reflection coefficient delivered by the single element without any impact neither on the operating bandwidths nor the resonant frequencies. Besides, a good matching is noticed along the working bands where the TARC is less than -10 dB. The fastness of the TARC is due to the quite weak mutual coupling lower than -30 dB among all elements and the insignificant differences between the curves is attributed to the different phases taken in each case, where case-3 yields the optimum TARC result. Consequently, the suggested MIMO antenna has proved the rigidity and strength of the working bandwidths in facing the diverse excitation phases.

The channel capacity loss (CCL) is the next important metric to be investigated. The CCL describes the maximum acceptable threshold of the transmission loss in a high data rate transfer under which the signal can be reliably transmitted without considerable loss, which should not override the agreed limit of 0.4 bit/s/Hz [25]. The computation of the CCL is performed using Eq. (9) where α^R is the correlation matrix of the receiving antenna. The computed CCL between each two elements is presented in Fig. 16c. As shown, the CCL is less than 0.35 bit/s/Hz throughout both bandwidths which respects the agreed criteria so the proposed MIMO may enables a reliable transmission.

$$C_{loss} = -\log_2 \det(\alpha^R) \tag{9}$$

Where $\alpha^R = \begin{bmatrix} \alpha_{ii} & \alpha_{ij} \\ \alpha_{ji} & \alpha_{jj} \end{bmatrix}$, $\alpha_{ii} = 1 - \left(|S_{ii}|^2 + |S_{ij}|^2 \right)$, and $\alpha_{ij} = -\left(S_{ii}^* S_{ij} + S_{ji}^* S_{jj} \right)$

Moreover, in order to further investigate the MIMO antenna performance, the calculated channel capacity of the proposed 4×4 MIMO antenna is plotted and compared with that of an ideal 4×4 MIMO system in Fig. 16d. The channel capacity (CC) defines the upper bound limit on the transmission rate at which the information signal transmission can be done reliably over the communication channel. The CC can be calculated based on Eq. (10) where I_{n_R} is the identity matrix, n_R/n_T is the number of receive/ transmit antennas, H_{scale} is the channel transfer matrix determined using Eq. (11), $\rho_{scale,RX}$ / $\rho_{scale,TX}$ are the receive/ transmit correlation matrix which take into account the impact of total efficiencies of the MIMO antenna elements and H_{iid} is the channel matrix modeled by the independent and identically distributed (i.i.d.) Rayleigh fading environment [26]. The four elements of the proposed MIMO antenna are considered as receiving antennas while the four transmitting antennas are assumed uncorrelated with prefect efficiency (100%). The channel capacity calculation is done by averaging 10,000 realizations of the Rayleigh

fading channel with a SNR of 20dB. As revealed in Fig. 16d, an ideal 4×4 MIMO system reaches a maximum channel capacity of about 23 bit/s/Hz [27]. Whereas the channel capacity of the proposed MIMO antenna is greater than 20.5 and 21 bit/s/Hz over the two operating bandwidths respectively and attains a maximum value around 22 bit/s/Hz at both resonating frequencies which approximately reaches 95% of the upper limit for the ideal case. Accordingly, the suggested 4×4 MIMO antenna shows a high channel capacity performance in a fading environment where the upper limit reached is extremely close to that of the ideal 4×4 MIMO system fixed at 23 bit/s/Hz, so high transmission rates can be delivered.

$$CC = E \left\{ \log_2 \det \left(I_{n_R} + \frac{SNR}{n_T} H_{scale} H_{scale}^T \right) \right\} \tag{10}$$

$$H_{scale} = \sqrt{\rho_{scale,RX}} H_{iid} \sqrt{\rho_{scale,TX}} \tag{11}$$

4 Performance comparison with the state of the art

In an effort to highlight the outcomes of the executed work, a detailed comparison of the suggested MIMO antenna with the other recent published works is brought in Table 2. As shown, there are certainly several MIMO antenna designs that have been reported in the state-of-the-art as candidates for the 5G millimeter wave applications at the most prominent bands 28/38 GHz. However, the MIMO antenna design suggested in this research outperformed the mentioned works in many key points. Indeed, the proposed MIMO antenna is distinguished by the smallest size and the highest isolation leading to achieve the lowest ECC and the minimum CCL, besides a stellar performance with desirable value in terms of DG, TARC and channel capacity (CC). Whereas, most cited works are not analyzed in terms of TARC, CCL and CC. Moreover, the MIMO elements are marked with the uppermost radiation efficiency and maintain a good comparable gain level without referring to any gain improvement technique. In addition to bearing a large bandwidth at both resonant frequencies while keeping a quite simple structure. As a result, the suggested MIMO antenna shows an impressive achievements qualifying it to be a robust contender and pretty convenient for the integration in 5G wireless devices.

5 Conclusions

In this manuscript, a novel four-element planar MIMO antenna has been carefully analyzed for the employment in 5G applications at millimeter wave spectrum. The proposed

Table 2 Evaluation of the proposed MIMO antenna performance versus the various reported works

Ref.	Size (mm ³)	Ports	Operating Frequency (GHz)	Operat. BW (GHz)	Max. gain (dB)	Efficiency (%)	Isolation (dB)	ECC/DG(dB)	TARC (dB)	CCL/CC (bit/s/Hz)
[1]	32.5×32.5×1.6	4	36.86–40	3.14	6.5	> 80	> 25	< 0.001/ > 9.99	NA	< 2/ NA
[3]	24×22.5×0.508	4	28 38	1 1.2	7.5	> 85	> 27	< 0.001/ NA	NA	NA
[8]	30×35×0.76	4	25.5–29.6	4.1	8.3	> 79	> 17	< 0.01/ > 9.96	NA	< 0.4/ NA
[10]	33×27.5×0.76	2	28	0.4	6.9	87% (at 28 GHz)	> 17	< 0.2/ > 9.7	NA	NA
[11]	30×30×0.8	4	28	2	6	> 89	> 29	< 0.16/ NA	NA	NA
[12]	80×80×1.57	4	23–40	17	12	> 85	> 20	< 0.012/ NA	NA	NA
[14]	14×26×0.38	2	28 38	2.55 2.1	1.83	> 76	> 20	< 0.001/ > 9.99	NA	< 0.4/ NA
[15]	26×11mm ²	2	27 39	4 4	5.7	> 97	> 20	< 0.001/ > 9.99	NA	NA
[19]	55×110×0.5	4	28 38	1.06 1.43	8.2	> 88.28	> 26	< 0.001/ NA	NA	NA
[21]	35×35×4.75	4	24.8–28.5 33.5–37	3.7 3.5	9.9	> 96	> 17	< 0.15/ > 9.97	< -10	< 0.6/ NA
[28]	41.5×10×0.8	4	28 38	1.39 3.33	5.7	> 80	> 25	< 0.001/ > 9.96	NA	NA
[29]	20×20×2.8	2	28	1.34	9	NA	> 24	< 0.013/ > 9.9	< -5	NA/ > 10
[30]	30×30×0.8	4	28	3	6.8	> 89	> 17	< 0.0015/ > 9.9	NA	NA
[31]	NA	4	24 28.5	1.53 4.5	4.9	> 90	> 27	NA	NA	NA
This work	14×14×0.8	4	28 38	3 3.2	6.8	> 98	> 30	< 0.0005/ > 9.99	< -10	< 0.35/ 22

design was featured with simple, compact, and quite small structure of $14 \times 14 \times 0.8 \text{ mm}^3$, resonated at 28/38 GHz using the proper geometric modifications and allowed dual-wideband characteristic with about 3 GHz at each band. The elements were characterized with directive patterns, high radiation efficiency up to 99% and a maximum gain of 6.8dB which proved a good radiation performance. Throughout this research, we have aimed to provide a high isolated MIMO elements without increasing the total size, thing that are successfully accomplished using polarization diversity and decoupling structure. In this way, a very high isolation out-paced 30 dB has been assured between all elements resulting in very good diversity performance which was examined by calculating various parameters such as the ECC, DG, TARC, CCL and channel capacity (CC). All the calculated parameters showed an excellent behavior and perfectly respected the practical limits along the two bands which would allow reliable connection with high data rate. Moreover, a comparison with the other related works emphasized that the suggested MIMO antenna combines a set of the most important features that make it a strong candidate and highly appropriate for the integration in wireless 5G equipments.

Authors' contributions Not Applicable.

Funding No funding was received for the submitted work.

Availability of data and material This work has no associated data.

Code Availability Not Applicable.

Declaration

Conflict of interest The authors declare no conflicts of interests.

References

- Sehrai, D. A., Asif, M., Shoaib, N., Ibrar, M., Jan, S., Alibakhshikenari, M. ... Limiti, E. (2021). Compact quad-element high-isolation wideband MIMO antenna for mm-wave applications. *Electronics*, 10(11), 1300. <https://doi.org/10.3390/electronics10111300>
- Shamim, S. M., Dina, U. S., Arafin, N., & Sultana, S. (2021). Design of efficient 37 GHz millimeter wave microstrip patch antenna for 5G mobile application. *Plasmonics*, 16, 1417–1425. <https://doi.org/10.1007/s11468-021-01412-x>
- Raheel, K., Altaf, A., Waheed, A., Kiani, S. H., Sehrai, D. A., Tubbal, F., & Raad, R. (2021). E-shaped H-slotted dual band mmwave antenna for 5G technology. *Electronics*, 10(9), 1019. <https://doi.org/10.3390/electronics10091019>
- Abdullah, M., Kiani, S. H., & Iqbal, A. (2019). Eight element multiple-input multiple-output (MIMO) antenna for 5G mobile applications. *IEEE Access*, 7, 134488–134495. <https://doi.org/10.1109/ACCESS.2019.2941908>
- Khan, J., Sehrai, D. A., Khan, M. A., Khan, H. A., Ahmad, S., Ali, A. ... Khan, S. (2019). Design and performance comparison of rotated Y-shaped antenna using different metamaterial surfaces for 5G mobile devices. *CMC- Computers, Materials & Continua*, 60, 409–420. <https://doi.org/10.32604/cmc.2019.06883>
- Zhang, P., Yang, B., Yi, C., Wang, H., & You, X. (2020). Measurement based 5G millimeter-wave propagation characterization in vegetated suburban macrocell environments. *IEEE Transactions on Antennas and Propagation*, 68(7), 5556–5567. <https://doi.org/10.1109/TAP.2020.2975365>
- Ullah, H., & Tahir, F. A. (2019). A broadband wire hexagon antenna array for future 5G communications in 28 GHz band. *Microwave and Optical Technology Letters*, 61(3), 696–701. <https://doi.org/10.1002/mop.31613>
- Khalid, M., Naqvi, S. I., Hussain, N., Rahman, M., Mirjavadi, S. S., Khan, M. J., & Amin, Y. (2020). 4-port MIMO antenna with defected ground structure for 5G millimeter wave applications. *Electronics*, 9(1), 71. <https://doi.org/10.3390/electronics9010071>
- Rangan, S., Rappaport, T. S., & Erkip, E. (2014). Millimeter-wave cellular wireless networks: potentials and challenges. *Proceedings of the IEEE*, 102(3), 366–385. <https://doi.org/10.1109/JPROC.2014.2299397>
- Usman, M., Kopal, E., Nasir, J., Zhu, Y., Yu, C., & Zhu, A. (2021). Compact SIW fed dual-port single element annular slot MIMO antenna for 5G mm wave applications. *IEEE Access*, 9, 91995–92002. <https://doi.org/10.1109/ACCESS.2021.3091835>
- Kamal, M. M., Yang, S., Ren, X. C., Altaf, A., Kiani, S. H., Anjum, M. R. ... Saeed, S. I. (2021). Infinity shell shaped MIMO antenna array for mm-wave 5G applications. *Electronics*, 10(2), 165. <https://doi.org/10.3390/electronics10020165>
- Sehrai, D. A., Abdullah, M., Altaf, A., Kiani, S. H., Muhammad, F., Tufail, M. ... Rahman, S. (2020). A novel high gain wideband MIMO antenna for 5G mm wave applications. *Electronics*, 9(6), 1031. <https://doi.org/10.3390/electronics9061031>
- Hussain, N., Jeong, M. J., Abbas, A., & Kim, N. (2020). Metasurface-based single-layer wideband circularly polarized MIMO antenna for 5G mm-wave systems. *IEEE Access*, 8, 130293–130304. <https://doi.org/10.1109/ACCESS.2020.3009380>
- Hasan, M. N., Bashir, S., & Chu, S. (2019). Dual band omnidirectional millimeter wave antenna for 5G communications. *Journal of Electromagnetic Waves and Applications*, 33(12), 1581–1590. <https://doi.org/10.1080/09205071.2019.1617790>
- Ali, W., Das, S., Medkour, H., & Lakrit, S. (2021). Planar dual-band 27/39 GHz millimeter-wave MIMO antenna for 5G applications. *Microsystem Technologies*, 27(1), 283–292. <https://doi.org/10.1007/s00542-020-04951-1>
- Desai, A., Bui, C. D., Patel, J., Upadhyaya, T., Byun, G., & Nguyen, T. K. (2020). Compact wideband four element optically transparent MIMO antenna for mm-wave 5G applications. *IEEE Access*, 8, 194206–194217. <https://doi.org/10.1109/ACCESS.2020.3033314>
- Tariq, S., Naqvi, S. I., Hussain, N., & Amin, Y. (2021). A metasurface-based MIMO antenna for 5G mm-wave applications. *IEEE Access*, 9, 51805–51817. <https://doi.org/10.1109/ACCESS.2021.3069185>
- Jilani, S. F., & Alomainy, A. (2018). Millimetre-wave T-shaped MIMO antenna with defected ground structures for 5G cellular networks. *IET Microwaves, Antennas & Propagation*, 12(5), 672–677. <https://doi.org/10.1049/iet-map.2017.0467>
- Marzouk, H. M., Ahmed, M. I., & Abdel-Shaalan, A. H. (2019). Novel dual-band 28/38 GHz MIMO antennas for 5G mobile applications. *Progress In Electromagnetics Research C*, 93, 103–117. <https://doi.org/10.2528/PIERC19032303>
- Kamal, M. M., Yang, S., Kiani, S. H., Sehrai, D. A., Alibakhshikenari, M., Abdullah, M. ... Munir, M. (2021). A novel hook-shaped antenna operating at 28 GHz for future 5G mm wave applications. *Electronics*, 10(6), 673. <https://doi.org/10.3390/electronics10060673>
- Girjashankar, P. R., & Upadhyaya, T. (2021). Substrate integrated waveguide fed dual band quad-elements rectangular dielectric resonator MIMO antenna for millimeter wave 5G wireless communication systems. *AEU – International Journal of Electronics*

and Communications, 137, 153821. <https://doi.org/10.1016/j.aeue.2021.153821>

22. Gupta, M., Mutai, K. K., Mathur, V., & Bhatnagar, D. (2020). A novel elliptical ring microstrip patch antenna for ultra-wideband applications. *Wireless Personal Communications*, 114, 3017–3029. <https://doi.org/10.1007/s11277-020-07515-8>
23. Alibakhshikenari, M., Babaieian, F., Virdee, B. S., Aïssa, S., Azpilicueta, L., See, C. H. ... Limiti, E. (2020). A comprehensive survey on “Various decoupling mechanisms with focus on metamaterial and metasurface principles applicable to SAR and MIMO antenna systems. *IEEE Access*, 8, 192965–193004. <https://doi.org/10.1109/ACCESS.2020.3032826>
24. Varshney, G., Gotra, S., Pandey, V. S., & Yaduvanshi, R. S. (2019). Proximity-coupled two-port multi-input-multi-output graphene antenna with pattern diversity for THz applications. *Nano Communication Networks*, 21, 100246. <https://doi.org/10.1016/j.nancom.2019.05.003>
25. Kumar, A., Ansari, A. Q., Kanaujia, B. K., & Kishor, J. (2019). A novel ITI-shaped isolation structure placed between two-port CPW-fed dual-band MIMO antenna for high isolation. *AEU – International Journal of Electronics and Communications*, 104, 35–43. <https://doi.org/10.1016/j.aeue.2019.03.009>
26. Parchin, N. O., Basherlou, H. J., Al-Yasir, Y. I. A., Abdulkhaleq, A. M., & Abd-Alhameed, R. A. (2020). Ultra-wideband diversity MIMO antenna system for future mobile handsets. *Sensors*, 20(8), 2371. <https://doi.org/10.3390/s20082371>
27. Li, Y., Zou, H., Wang, M., Peng, M., & Yang, G. (2018). Eight-element MIMO antenna array for 5G/Sub-6GHz indoor micro wireless access points. In *2018 International Workshop on Antenna Technology (iWAT)*, Nanjing, China, (pp. 1–4). IEEE. <https://doi.org/10.1109/IWAT.2018.8379170>
28. Rafique, U., Agarwal, S., Nauman, N., Khalil, H., & Ullah, K. (2021). Inset-fed planar antenna array for dual-band 5G MIMO applications. *Progress In Electromagnetics Research C*, 112, 83–98. <https://doi.org/10.2528/PIERC21021302>
29. Zhang, Y., Deng, J. Y., Li, M. J., Sun, D., & Guo, L. X. (2019). A MIMO dielectric resonator antenna with improved isolation for 5G mm-wave applications. *IEEE Antennas and Wireless Propagation Letters*, 18(4), 747–751. <https://doi.org/10.1109/LAWP.2019.2901961>
30. Rahman, S., Ren, X. C., Altaf, A., Irfan, M., Abdullah, M., Muhammad, F. ... AlKahtani, F. S. (2020). Nature inspired MIMO antenna system for future mmWave technologies. *Micromachines*, 11(12), 1083. <https://doi.org/10.3390/mi11121083>
31. Aboualalaa, M., Mansour, I., Elsadek, H., Abdel-Rahman, A. B., Allam, A., Abo-Zahhad, M. ... Pokharel, R. K. (2019). Independent matching dual-band compact quarter-wave half-slot antenna for millimeter-wave applications. *IEEE Access*, 7, 130782–130790. <https://doi.org/10.1109/ACCESS.2019.2940273>

Publisher's note Springer Nature remains neutral with regard to jurisdictional claims in published maps and institutional affiliations.



Asma Khabba is currently pursuing the studies toward the Ph.D. degree in telecommunication and signal processing in Cady Ayyad University, Marrakech, Morocco. She received the bachelor of sciences in physics and the Master degree in control, industrial computing, signals and systems in 2015 and 2017 respectively from Cadi Ayyad University. Her research interests include 5G antenna, microwave/millimeter wave antenna, phased array and MIMO antenna.



Jamal Amadid is currently a PhD student at Cadi Ayyad University (UCA), Marrakesh, Morocco. He got the Bachelor of Sciences in physics and the Master's degree in control, industrial computing, signals and systems from UCA in 2016 and 2019 respectively. His main research interests are: Massive-MIMO network, Channel Estimation for spatial correlated channels, pilot contamination and the cell-free Massive-MIMO in the 5G wireless communications system.



Saida Ibnnyaich is currently a professor at Cadi Ayyad University, Marrakesh, Morocco. She received the Bachelor degree in technical sciences, the Master degree in Electrical Engineering, Power Electronics and Industrial Control and the PhD degree in computing and telecommunication in 2002, 2005, and 2013 respectively from Cadi Ayyad University. Her research interest includes telecommunications, microwaves, millimeter waves, PIFA antenna and patch antenna.



Abdelouhab Zeroual is a professor of telecommunication systems and signal processing. He is the head of Instrumentation, signals and systems Team at the Faculty of Sciences Sémalalia, Cadi Ayyad University in Marrakesh, Morocco. He received the Ph.D. degree in 1995 from Cadi Ayyad University. He is supervising several research works and a reviewer in several international journals. His research interest includes instrumentation, solar energy, signal processing and wireless communications. He has published more than 140 conference papers and more than 60 journal papers.